

Some effects of horizontal discretization on linear baroclinic and symmetric instabilities

William Barham^b, Scott Bachman^a, Ian Grooms^{b,*}

^a*Climate and Global Dynamics Division, National Center for Atmospheric Research, 1850 Table Mesa Drive, Boulder, CO 80305, USA*

^b*Department of Applied Mathematics, University of Colorado, Boulder, CO 80309, USA*

Abstract

The effects of horizontal discretization on linear baroclinic and symmetric instabilities are investigated by analyzing the behavior of the hydrostatic Eady problem in ocean models on the B and C grids. On the C grid a spurious baroclinic instability appears at small wavelengths. This instability does not disappear as the grid scale decreases; instead, it simply moves to smaller horizontal scales. The peak growth rate of the spurious instability is independent of the grid scale as the latter decreases. It is equal to $cf/\sqrt{\text{Ri}}$ where Ri is the balanced Richardson number, f is the Coriolis parameter, and c is a nondimensional constant that depends on the Richardson number. As the Richardson number increases c increases towards an upper bound of approximately $1/2$; for large Richardson numbers the spurious instability is faster than the Eady instability. To suppress the spurious instability it is recommended to use fourth-order centered tracer advection along with biharmonic viscosity and diffusion with coefficients $(\Delta_x)^4 f / (32 \sqrt{\text{Ri}})$ or larger where Δ_x is the grid scale.

On the B grid, the growth rates of baroclinic and symmetric instabilities are too small, and converge upwards towards the correct values as the grid scale decreases; no spurious instabilities are observed. In B grid models at eddy-permitting resolution, the reduced growth rate of baroclinic instability may contribute to partially-resolved eddies being too weak. On the C grid the growth rate of symmetric instability is better (larger) than on the B grid, and converges upwards towards the correct value as the grid scale decreases.

Keywords: Baroclinic instability, symmetric instability, discretization

1. Introduction

The study of the effects of discretization on free wave propagation in models of geophysical fluids has a long history, dating at least to the work of Charney et al. (1950). In particular, the propagation of Rossby and inertia-gravity waves in the various

*Corresponding author
Email address: ian.grooms@colorado.edu (Ian Grooms)

staggered ‘Arakawa’ grids (Arakawa and Lamb, 1977) has received a great deal of attention over the years; many results are reviewed in Haidvogel and Beckmann (1999), including the seminal work of Wajsowicz (1986) and Dukowicz (1995). On the B grid, the horizontal components of velocity are staggered with respect to the tracers, but not with respect to each other; on the C grid they are staggered with respect to each other and with respect to the tracers. Intuition suggests and the aforementioned studies confirm that the B grid is more suited to describing large-scale geostrophic dynamics like Rossby waves than the C grid, and the B grid has been popular in models used to simulate the global ocean. The B grid is used by the Parallel Ocean Program (POP), which is the ocean model component of both the Community Climate System Models (CCSM; Gent et al., 2011) and the current version of the Community Earth System Model (CESM; Hurrell et al., 2013), and by the Modular Ocean Model (MOM5), which is the ocean component of the CM2.5 model (Delworth et al., 2012). (The next version of MOM will use the C grid.) Models used to simulate smaller-scale dynamics, e.g. in regional simulations and process studies, often use the C grid; examples include the Regional Ocean Modeling System (ROMS Shchepetkin and McWilliams, 2005), and the MITgcm (Marshall et al., 1997). The ocean component of the Nucleus for European Modelling of the Ocean (NEMO-OPA; Madec, 2008) also uses the C grid, which may become more popular for global models as resolution increases.

The distinction between these model grid types, and their relative advantages and disadvantages, is important because the steady increase in computational capacity at many climate modeling centers has ushered in a transitional period for global ocean models. Previous IPCC-class models have been limited to horizontal resolutions $\geq 1^\circ$, which is insufficient to resolve oceanic mesoscale eddies. Increasing resolution from the 1° benchmark means that mesoscale eddies will be resolved naturally across some of the global ocean, promising increased realism of the global circulation (e.g. Maltrud and McClean, 2005; Kirtman et al., 2012; Hallberg, 2013; Graham, 2014; Treguier et al., 2014) and improved coupling to other components of the climate system (e.g. Delworth et al., 2012; Frenger et al., 2013).

Progression into this “eddy-permitting” regime introduces a suite of new challenges, among which is the issue of how the structure of the model grid affects the growth and behavior of the mesoscale eddies themselves. These eddies are geostrophically balanced, which suggests that they might be more accurately represented on a B grid, but they are not linear Rossby waves so the above-referenced free-wave analyses do not directly apply. Direct analysis of the effects of numerical discretization on nonlinear mesoscale eddy dynamics is not straightforward, and a different approach – linear, yet hopefully relevant to mesoscale eddy dynamics – is taken here. Mesoscale eddies are believed to sustain their energy primarily by extracting available potential energy from the large-scale flow (e.g. Ferrari and Wunsch, 2009), and a canonical linear model for this process is baroclinic instability. In this paper we study the effects of discretization on the properties of linear baroclinic instability in the Eady problem. We use hydrostatic dynamics, as typically used by global ocean models, and consider commonly-used discretizations on the B and C grids. Since the symmetric instability arises in the Eady problem in addition to the baroclinic instability, the behavior of symmetric instability under discretization is also investigated.

The paper is organized as follows. The hydrostatic ocean primitive equations, the

spatial grids, and the discretizations of interest are described in section 2. Linear perturbation equations for the Eady problem under the different discretizations are derived in section 3. Growth rates of symmetric and baroclinic instabilities for the discretized models are presented in section 4. Section 4.4 investigates the causes of and remedies for the spurious baroclinic instability on the C grid, and section 4.5 verifies the linear analysis by comparison to direct simulations of the nonlinear equations. Some conclusions are discussed in section 5.

2. Preliminaries & Notation

2.1. Governing Partial Differential Equations

The inviscid, hydrostatic primitive equations on an f -plane are

$$\partial_t u + \mathbf{u} \cdot \nabla u - f_0 v = -\partial_x p \quad (1)$$

$$\partial_t v + \mathbf{u} \cdot \nabla v + f_0 u = -\partial_y p \quad (2)$$

$$\partial_t b + \mathbf{u} \cdot \nabla b = 0 \quad (3)$$

$$\nabla \cdot \mathbf{u} = 0, \quad (4)$$

$$\partial_z p = b. \quad (5)$$

The velocity is $\mathbf{u} = (u, v, w)$, f_0 is the Coriolis parameter, and b is the buoyancy. The pressure p has been rescaled by a constant reference density ρ_0 , and the Boussinesq approximation has been used.

The depth-independent (barotropic) component of pressure is not constrained by Eq. (5). We will here use a rigid-lid approximation to constrain the barotropic pressure. To wit, the depth-average of Eq. (4) is

$$\partial_x U + \partial_y V = 0$$

where U and V are the depth-averaged components of u and v , and the vertical velocity w has been set to zero at both boundaries. The depth-averages of Eqs. (1) and (2) are

$$\partial_t U + H^{-1} \int_0^H \mathbf{u} \cdot \nabla u \, dz - f_0 V = -\partial_x \phi$$

$$\partial_t V + H^{-1} \int_0^H \mathbf{u} \cdot \nabla v \, dz + f_0 U = -\partial_y \phi$$

where H is the depth and ϕ is the barotropic pressure. Taking the divergence of these equations leads to an elliptic equation for the barotropic pressure

$$\nabla_h^2 \phi = f_0 (\partial_x V - \partial_y U) - H^{-1} \nabla_h \cdot \int_0^H \mathbf{u} \cdot \nabla \mathbf{u} \, dz \quad (6)$$

where $\nabla_h = (\partial_x, \partial_y)$.

The above derivation applies at the level of the partial differential equations. It bears noting that typical discrete ocean models allow for the existence of a divergent

barotropic mode, e.g. in the initial condition. In the context of a discrete ocean model, the above condition on the barotropic pressure does not prevent a divergent barotropic mode from *existing*, it simply prevents it from *evolving*.

2.2. Notation for discretized equations

We wish to investigate the dynamics on a regular Cartesian grid with grid sizes Δ_x , Δ_y , and $\Delta_z = H/N_z$, where N_z is the number of vertical levels. The velocity, pressure, and buoyancy will be tracked at points on the grid; vectors of their values on the grid will be denoted \mathbf{u} , \mathbf{v} , \mathbf{w} , \mathbf{p} , and \mathbf{b} . The vectors will be triply-indexed, e.g. $\mathbf{u}_{\{i,j,k\}}$, with indices i , j , and k denoting locations in the x , y , and z directions, respectively. Indices are often truncated to save space, e.g. $\mathbf{u}_{\{i+1\}}$ is a shorthand for $\mathbf{u}_{\{i+1,j,k\}}$.

To isolate the effects of horizontal discretization, the vertical discretization will be kept uniform, with large N_z . The vertical discretization uses the Lorenz grid common to the ocean models referenced in the introduction (Lorenz, 1960): All variables except the vertical velocity are associated with the vertical grid points $(k - 1/2)\Delta_z$, $k = 1, \dots, N_z$. The vertical velocity is associated with the vertical grid points $k\Delta_z$, $k = 0, \dots, N_z$.

Variables on the B grid occur in one of two sets of horizontal locations: $\mathbf{b}_{\{i,j\}}$, $\mathbf{p}_{\{i,j\}}$, $\phi_{\{i,j\}}$, and $\mathbf{w}_{\{i,j\}}$ are located at $(x, y) = (\Delta_x i, \Delta_y j)$, while $\mathbf{u}_{\{i,j\}}$ and $\mathbf{v}_{\{i,j\}}$ are located at $(x, y) = (\Delta_x(i + 1/2), \Delta_y(j + 1/2))$. Variables on the C grid occur in one of three sets of horizontal locations. The buoyancy, vertical velocity, and tracer are all located at $(x, y) = (\Delta_x i, \Delta_y j)$ (same as the B grid), while $\mathbf{u}_{\{i,j\}}$ is located at $(x, y) = (\Delta_x(i+1/2), \Delta_y j)$ and $\mathbf{v}_{\{i,j\}}$ is located at $(x, y) = (\Delta_x i, \Delta_y(j + 1/2))$. On both grids the vertical velocity is staggered with respect to the other variables. The convention adopted here is to place $\mathbf{w}_{\{k\}}$ at $z = k\Delta_z$, and all the other variables at $z = (k - 1/2)\Delta_z$.

The methods used to discretize the governing equations can be completely described in terms of a few fundamental average and difference operators. These operators are defined below according to their action

$$[a_x^\pm \mathbf{u}]_{\{i\}} = \frac{\mathbf{u}_{\{i\pm 1\}} + \mathbf{u}_{\{i\}}}{2}, \quad [\delta_x^\pm \mathbf{u}]_{\{i\}} = \pm \frac{\mathbf{u}_{\{i\pm 1\}} - \mathbf{u}_{\{i\}}}{\Delta_x} \quad (7)$$

$$[a_y^\pm \mathbf{u}]_{\{j\}} = \frac{\mathbf{u}_{\{j\pm 1\}} + \mathbf{u}_{\{j\}}}{2}, \quad [\delta_y^\pm \mathbf{u}]_{\{j\}} = \pm \frac{\mathbf{u}_{\{j\pm 1\}} - \mathbf{u}_{\{j\}}}{\Delta_y} \quad (8)$$

$$[a_z^\pm \mathbf{u}]_{\{k\}} = \frac{\mathbf{u}_{\{k\pm 1\}} + \mathbf{u}_{\{k\}}}{2}, \quad [\delta_z^\pm \mathbf{u}]_{\{k\}} = \pm \frac{\mathbf{u}_{\{k\pm 1\}} - \mathbf{u}_{\{k\}}}{\Delta_k}. \quad (9)$$

It can be easily verified that all of these operators commute with one another, and the convention adopted here will be to list averages before differences, and plus before minus. Let the reader be advised that these operators are not centered! The usual centered differences can be recovered by the combination of a forward difference (δ^+) and a backward average (a^-), or a backward difference and a forward average.

2.3. Discrete formulation on the B Grid

The discrete momentum equations on the B grid have the form

$$\frac{d\mathbf{u}}{dt} + \mathbf{A}_u^B - f_0\mathbf{v} = -a_y^+\delta_x^+(\mathbf{p} + \phi) \quad (10)$$

$$\frac{d\mathbf{v}}{dt} + \mathbf{A}_v^B + f_0\mathbf{u} = -a_x^+\delta_y^+(\mathbf{p} + \phi) \quad (11)$$

where \mathbf{A}_u^B and \mathbf{A}_v^B are discretizations of advection of zonal and meridional momentum, respectively, and \mathbf{p} and ϕ are the baroclinic and barotropic pressures, respectively. The dependent variables \mathbf{u} and \mathbf{v} in Eq. (10) and (11) are vectors of the values of u and v on the computational grid; as a result, they are systems of ordinary rather than partial differential equations. The second-order, energy-conserving discretization of momentum advection due to Bryan (1969) is somewhat complicated. To save space, define the following averaged velocity components

$$\mathbf{u}^* = a_x^+a_y^+a_y^-\mathbf{u} \quad (12)$$

$$\mathbf{v}^* = a_x^+a_x^-a_y^+\mathbf{v} \quad (13)$$

$$\mathbf{w}^* = a_x^+a_y^+\mathbf{w}. \quad (14)$$

With this notation, the zonal momentum advection takes the form

$$\mathbf{A}_u^B = \delta_x^- [\mathbf{u}^*(a_x^+\mathbf{u})] + \delta_y^- [\mathbf{v}^*(a_y^+\mathbf{u})] + \delta_z^- [\mathbf{w}^*(a_z^+\mathbf{u})]. \quad (15)$$

The meridional momentum advection has the same form but with \mathbf{v} replacing \mathbf{u} .

The standard second-order discretization of the tracer advection on the B grid takes the form

$$\delta_x^- [(a_y^-\mathbf{u})(a_x^+\mathbf{b})] + \delta_y^- [(a_x^-\mathbf{v})(a_y^+\mathbf{b})] + \delta_z^- [\mathbf{w}(a_z^+\mathbf{b})]. \quad (16)$$

The discrete continuity equation is obtained by applying the tracer advection to a constant buoyancy profile $\mathbf{b} = 1$,

$$a_y^-\delta_x^-\mathbf{u} + a_x^-\delta_y^-\mathbf{u} + \delta_z^-\mathbf{w} = 0. \quad (17)$$

The discrete hydrostatic balance is simply

$$\delta_z^+\mathbf{p} = a_z^+\mathbf{b}. \quad (18)$$

This form of discrete hydrostatic balance has been shown to preserve the total (kinetic plus potential) energy by Bryan (1969). The equation for discrete barotropic pressure is obtained by a derivation analogous to the derivation for the continuous equations. It is unwieldy, and not presented here. A derivation for the much simpler case of a normal-mode perturbation is in Appendix A.

2.4. Discrete formulation on the C Grid: Flux-Form

The discrete momentum equations on the C grid have the form

$$\frac{d\mathbf{u}}{dt} + \mathbf{A}_u^C - f_0 a_x^+ a_y^- \mathbf{v} = -\delta_x^+ (\mathbf{p} + \phi) \quad (19)$$

$$\frac{d\mathbf{v}}{dt} + \mathbf{A}_v^C + f_0 a_x^- a_y^+ \mathbf{u} = -\delta_y^+ (\mathbf{p} + \phi) \quad (20)$$

where \mathbf{A}_u^C and \mathbf{A}_v^C are discretizations of zonal and meridional momentum advection, respectively. Note that, compared to the B grid, the Coriolis terms are now averaged but the pressure gradient is not. The B grid nevertheless requires fewer averaging operators than the C grid, which suggests that the B grid will more accurately represent geostrophic flows at large scales that balance the Coriolis acceleration and the pressure gradient. The second-order, energy-conserving, flux-form discretization of momentum advection on the C grid takes the form

$$\mathbf{A}_u^C = \delta_x^- \left[\frac{(a_x^+ \mathbf{u})^2}{2} \right] + \delta_y^- \left[(a_x^+ \mathbf{v})(a_y^+ \mathbf{u}) \right] + \delta_z^- \left[(a_x^+ \mathbf{w})(a_z^+ \mathbf{u}) \right]. \quad (21)$$

and the meridional momentum advection takes the form

$$\mathbf{A}_v^C = \delta_x^- \left[(a_y^+ \mathbf{u})(a_x^+ \mathbf{v}) \right] + \delta_y^- \left[\frac{(a_y^+ \mathbf{v})^2}{2} \right] + \delta_z^- \left[(a_y^+ \mathbf{w})(a_z^+ \mathbf{v}) \right]. \quad (22)$$

The standard second-order discretization of the tracer advection on the C grid takes the form

$$\delta_x^- \left[\mathbf{u}(a_x^+ \mathbf{b}) \right] + \delta_y^- \left[\mathbf{v}(a_y^+ \mathbf{b}) \right] + \delta_z^- \left[\mathbf{w}(a_z^+ \mathbf{b}) \right]. \quad (23)$$

The discrete continuity equation is again obtained by applying the tracer advection to a constant buoyancy profile $\mathbf{b} = 1$,

$$\delta_x^- \mathbf{u} + \delta_y^- \mathbf{v} + \delta_z^- \mathbf{w} = 0. \quad (24)$$

The discrete hydrostatic balance is the same as Eq. (18), and a barotropic pressure equation for a normal-mode perturbation is derived in Appendix A.

2.5. Discrete formulation on the C Grid: Vector-Invariant

The horizontal advection of momentum in the primitive equations can be written in vector-invariant form as

$$u\partial_x u + v\partial_y u = \frac{1}{2}\partial_x(u^2 + v^2) - \zeta v \quad (25)$$

$$u\partial_x v + v\partial_y v = \frac{1}{2}\partial_y(u^2 + v^2) + \zeta u \quad (26)$$

where $\zeta = \partial_x v - \partial_y u$ is the vertical component of relative vorticity. We consider two discretizations using this form: an enstrophy-conserving form ENS from Sadourny (1975) and an energy and enstrophy conserving form called EEN (see, e.g. Arakawa and Lamb (1981), Madec (2008), and Le Sommer et al. (2009)). The ENS discretization of equations (25) and (26) takes the form

$$\frac{1}{2}\partial_x(u^2 + v^2) - \zeta v \approx \frac{1}{2}\delta_x^+ (a_x^-(\mathbf{u}^2) + a_y^-(\mathbf{v}^2)) - (a_y^-(\delta_x^+ \mathbf{v} - \delta_y^+ \mathbf{u}))(a_x^+ a_y^- \mathbf{v}) \quad (27)$$

$$\frac{1}{2}\partial_y(u^2 + v^2) + \zeta u \approx \frac{1}{2}\delta_y^+ (a_x^-(\mathbf{u}^2) + a_y^-(\mathbf{v}^2)) + (a_x^-(\delta_x^+ \mathbf{v} - \delta_y^+ \mathbf{u}))(a_x^- a_y^+ \mathbf{u}) \quad (28)$$

The EEN form is significantly more complicated. The gradient of horizontal kinetic energy remains the same, but the product of relative vorticity and velocity takes the form

$$\begin{aligned} \zeta v \approx \frac{1}{12} & \left[(\omega_{\{i,j\}} + \omega_{\{i,j-1\}} + \omega_{\{i-1,j\}}) \mathbf{v}_{\{i,j\}} \right. \\ & + (\omega_{\{i,j\}} + \omega_{\{i,j-1\}} + \omega_{\{i-1,j-1\}}) \mathbf{v}_{\{i,j-1\}} \\ & + (\omega_{\{i,j\}} + \omega_{\{i,j-1\}} + \omega_{\{i+1,j\}}) \mathbf{v}_{\{i+1,j\}} \\ & \left. + (\omega_{\{i,j\}} + \omega_{\{i,j-1\}} + \omega_{\{i+1,j-1\}}) \mathbf{v}_{\{i+1,j-1\}} \right] \end{aligned} \quad (29)$$

$$\begin{aligned} \zeta u \approx \frac{1}{12} & \left[(\omega_{\{i,j\}} + \omega_{\{i-1,j\}} + \omega_{\{i,j-1\}}) \mathbf{u}_{\{i,j\}} \right. \\ & + (\omega_{\{i,j\}} + \omega_{\{i-1,j\}} + \omega_{\{i-1,j-1\}}) \mathbf{u}_{\{i-1,j\}} \\ & + (\omega_{\{i,j\}} + \omega_{\{i-1,j\}} + \omega_{\{i,j+1\}}) \mathbf{u}_{\{i,j+1\}} \\ & \left. + (\omega_{\{i,j\}} + \omega_{\{i-1,j\}} + \omega_{\{i-1,j+1\}}) \mathbf{u}_{\{i-1,j+1\}} \right] \end{aligned} \quad (30)$$

where $\omega_{\{i,j\}} = \delta_x^+ \mathbf{v} - \delta_x^+ \mathbf{u}$.

3. Linear Perturbation Equations

The steady configuration

$$\begin{aligned} \bar{u}(z) &= -M^2(z - H/2)/f_0, \quad \bar{v} = \bar{w} = 0, \\ \bar{b} &= N^2 z + M^2 y \end{aligned} \quad (31)$$

is an exact solution of the governing equations (1)–(6). The Brunt-Väisälä frequency is N , and the slope of the isopycnals is M^2/N^2 ; the vertical shear is $-M^2/f_0$. The linear stability of this equilibrium to infinitesimal perturbations has been considered by

a legion of authors beginning with Eady (1949), and with notable contributions in the hydrostatic, non-geostrophic case by Stone (1966, 1970). The goal here is to study linear stability of the discretized equations. It is easy to verify that the following discrete configuration is also an equilibrium of the discretized equations (since a second-order discretization applied to a linear function is exact):

$$\bar{\mathbf{u}}_{\{i,j,k\}} = -\frac{M^2 \Delta_z}{f_0} \left(k - \frac{N_z + 1}{2} \right) \quad (32)$$

$$\bar{\mathbf{b}}_{\{i,j,k\}} = N^2 \Delta_z k + M^2 j \Delta_y \quad (33)$$

$$\bar{\mathbf{v}}_{\{i,j,k\}} = 0. \quad (34)$$

It is straightforward to derive linear perturbation equations about this equilibrium. On the B grid these have the following form

$$\frac{d\mathbf{u}'}{dt} + \bar{\mathbf{u}}(a_x^+ \delta_x^- \mathbf{u}') - \frac{M^2 a_x^+ a_y^+ a_z^-}{f_0} \mathbf{w}' - f_0 \mathbf{v}' = -a_y^+ \delta_x^+ (\mathbf{p}' + \phi') \quad (35)$$

$$\frac{d\mathbf{v}'}{dt} + \bar{\mathbf{u}}(a_x^+ \delta_x^- \mathbf{v}') + f_0 \mathbf{u}' = -a_x^+ \delta_y^+ (\mathbf{p}' + \phi') \quad (36)$$

$$\frac{d\mathbf{b}'}{dt} + \bar{\mathbf{u}}(a_x^+ \delta_x^- \mathbf{b}') + N^2 a_z^- \mathbf{w}' + M^2 a_x^- a_y^- \mathbf{v}' = 0. \quad (37)$$

The system is completed by the discrete incompressibility condition on the B grid, Eq. (17), and the discrete hydrostatic balance, Eq. (18). Note that the above equations are to be interpreted as holding at index $\{i, j, k\}$.

The discrete system governing linear perturbations on the C grid with the flux-form and vector-invariant ENS forms of the momentum equations has the form

$$\frac{d\mathbf{u}'}{dt} + \bar{\mathbf{u}}(a_x^+ \delta_x^- \mathbf{u}') - \frac{M^2 a_x^+ a_z^-}{f_0} \mathbf{w}' - f_0 a_x^+ a_y^- \mathbf{v}' = -\delta_x^+ (\mathbf{p}' + \phi') \quad (38)$$

$$\frac{d\mathbf{v}'}{dt} + \bar{\mathbf{u}}(a_x^+ \delta_x^- \mathbf{v}') + f_0 a_x^- a_y^+ \mathbf{u}' = -\delta_y^+ (\mathbf{p}' + \phi') \quad (39)$$

$$\frac{d\mathbf{b}'}{dt} + \bar{\mathbf{u}}(a_x^+ \delta_x^- \mathbf{b}') + N^2 a_z^- \mathbf{w}' + M^2 a_y^- \mathbf{v}' = 0. \quad (40)$$

The system is completed by the discrete incompressibility condition on the C grid, Eq. (24), and by the discrete hydrostatic balance, Eq. (18).

The linear perturbation equations for with the EEN vector-invariant discretization (Madec, 2008; Le Sommer et al., 2009) only differ in the meridional momentum equa-

tion, which takes the following form

$$\frac{d\mathbf{v}'}{dt} + \bar{\mathbf{u}} \frac{1}{3} (1 + 2a_y^+ a_y^-) (a_x^+ \delta_x^- \mathbf{v}') + f_0 a_x^- a_y^+ \mathbf{u}' - \bar{\mathbf{u}} \frac{\Delta_y^2}{6} (\delta_y^+)^2 \delta_y^- \mathbf{u}' = -\delta_y^+ (\mathbf{p}' + \phi'). \quad (41)$$

The final term on the left hand side is purely dispersive and converges towards zero as the grid is refined. For perturbations on the baroclinic axis, i.e. with no variation in the meridional direction, the linear perturbation equation is the same as in the ENS and flux-form cases since $a_y^\pm \rightarrow 1$ and $\delta_y^\pm \rightarrow 0$. For perturbations on the symmetric axis, i.e. with no variation in the zonal direction, the term $(a_x^+ \delta_x^-) \mathbf{v}' \rightarrow 0$ but the final term dispersive term on the left-hand side remains. For this reason the EEN vector-invariant form is only considered separately from the other C grid discretizations in the examination of symmetric instability.

On both grids, as in the continuous problem, the background state does not vary in the horizontal. Thus, as in the continuous problem, the linear perturbation equations can be resolved into normal modes that are simply Fourier modes. Solutions are therefore sought in the form

$$\mathbf{u}' = \hat{\mathbf{u}} e^{i(k_x \Delta_x + k_y \Delta_y j)} + \text{complex conjugate} \quad (42)$$

with similar representations of the other variables (note the notational distinction between $\sqrt{-1} = i$ and the index i). The coefficient vector $\hat{\mathbf{u}}$ is now a singly-indexed vector with index k varying across the depth. By considering the domain to be of infinite horizontal extent, all wavenumbers up to the Nyquist are admissible on the grid:

$$(k_x, k_y) \in \left[-\frac{\pi}{\Delta_x}, \frac{\pi}{\Delta_x} \right] \times \left[-\frac{\pi}{\Delta_y}, \frac{\pi}{\Delta_y} \right]. \quad (43)$$

The horizontal averaging and difference operators admit these discrete Fourier modes as eigenvectors, with the following eigenvalues

$$\hat{a}_x^\pm = \frac{e^{\pm i k_x \Delta_x} + 1}{2}, \quad \hat{\delta}_x^\pm = \pm \frac{e^{\pm i k_x \Delta_x} - 1}{\Delta_x} \quad (44)$$

$$\hat{a}_y^\pm = \frac{e^{\pm i k_y \Delta_y} + 1}{2}, \quad \hat{\delta}_y^\pm = \pm \frac{e^{\pm i k_y \Delta_y} - 1}{\Delta_y}. \quad (45)$$

The equations governing the linear evolution of a normal mode constitute a system of differential-algebraic equations: differential equations for $\hat{\mathbf{u}}$, $\hat{\mathbf{v}}$, and $\hat{\mathbf{b}}$ and algebraic equations for $\hat{\mathbf{w}}$, $\hat{\mathbf{p}}$, and $\hat{\phi}$. It is convenient to eliminate the three diagnostic variables to obtain a system of linear differential equations for the three prognostic variables. The details of this elimination can be found in Appendix A. The result in both cases is a

system of linear differential equations, i.e.

$$\frac{d}{dt} \begin{pmatrix} \hat{u} \\ \hat{v} \\ \hat{b} \end{pmatrix} = \mathbf{L} \begin{pmatrix} \hat{u} \\ \hat{v} \\ \hat{b} \end{pmatrix} \quad (46)$$

where the matrix \mathbf{L} takes different forms on the B and C grids. The matrix \mathbf{L} is $3N_z \times 3N_z$, and depends on the wavenumbers (k_x, k_y) , the grid scales Δ_x , Δ_y , and Δ_z , and the external parameters H , f_0 , N^2 , and M^2 . The linear stability analysis consists of computing the eigenvalue with the largest real part; if the real part is positive then the system is linearly unstable.

4. Discrete Growth Rates

The deformation radius is $NH/|f_0|$; rather than non-dimensionalize the system, we fix $H = 4000$ m, $N = 10^{-3}$ s $^{-1}$, and $f_0 = -10^{-4}$ s $^{-1}$, for a deformation radius of 40 km. After nondimensionalization (e.g. Stone (1966)) the linear stability problem depends only on the Richardson number, so results for other parameter values can be obtained by rescaling. The grid spacing will always be isotropic: $\Delta_x = \Delta_y$. Unless noted otherwise, $N_z = 128$.

Results of the linear stability analysis of the Eady problem are usually organized using the Richardson number, which (for the Eady problem) is $Ri = N^2 f_0^2 / M^4$. Summarizing the results of Stone (1966, 1970), for $Ri \gg 1$ the peak instability occurs on the ‘baroclinic’ axis $k_y = 0$ at a wavenumber k_x somewhat larger than the deformation wavenumber $|f_0|/(NH)$. $Ri \gg 1$ is the ‘quasigeostrophic’ regime investigated by Eady (1949), and the instability is ‘baroclinic.’ In this regime the peak growth rate scales approximately as $0.31M^2/N$. For $Ri \leq 1$ a new instability occurs with maximum growth rate on the ‘symmetric’ axis $k_x = 0$; for $Ri < 0.95$ this new ‘symmetric’ instability grows faster than the baroclinic instability. The symmetric instability in turn gives way to a Kelvin-Helmholtz instability at $Ri < 0.25$, but this parameter regime is not of interest here, being far from the current resolving capabilities of hydrostatic ocean models.

The correct eigenvalues, without errors due to horizontal discretization, can be obtained by taking the limit $\Delta_x, \Delta_y \rightarrow 0$. The limit is obtained by setting $\hat{a}_x^\pm = \hat{a}_y^\pm = 1$ and $\hat{\delta}_x^\pm = ik_x$, $\hat{\delta}_y^\pm = ik_y$.

4.1. Symmetric Instability

Figure 1 shows growth rates of symmetric instability at $Ri = 1/2$ for the B and C grids at grid sizes of 25, 12.5, 6.25, and 3.125 km; the Nyquist wavenumber for each grid size has been marked with an \times . The B grid does not have any unstable modes for grid sizes of 25 and 12.5 km. At 6.25 km there is a range of unstable modes but their growth rates are significantly too small, while at 3.125 km the largest-scale unstable modes are reasonably well represented. On the C grid there are unstable modes at every grid scale. As the grid scale decreases the discrete instability becomes more accurate: the range of unstable modes widens and the growth rates increase. These tendencies for the range and growth rates to increase as the grid scale decreases was also predicted

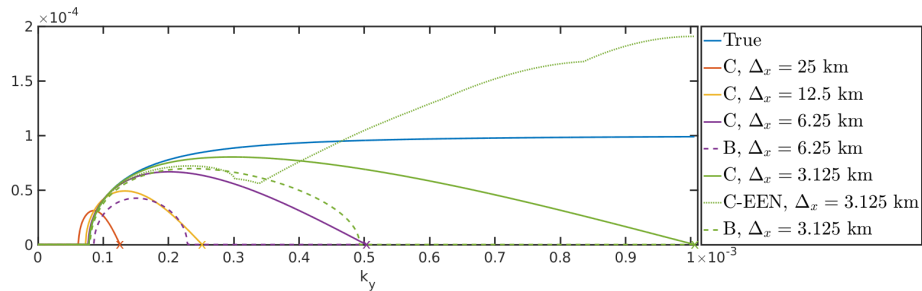


Figure 1: Growth rates of symmetric instability at $Ri = 1/2$ for grid sizes $\Delta_x = 25, 12.5, 6.25,$ and 3.125 km. Growth rates are shown in units of s^{-1} ; the wavenumber k_y has units of m^{-1} . All results were computed using $N_z = 128$. The Nyquist wavenumbers for all grid sizes are marked with \times at the end of the growth rate curves. The blue line shows the true growth rate, obtained by taking $\Delta_x \rightarrow 0$. No results are shown for the B grid at $\Delta_x = 25$ and 12.5 km since the code is stable at those grid scales. The dotted green line shows the growth rate on the C grid with grid size 3.125 km and the vector-invariant EEN discretization.

by Bachman and Taylor (2014) for the case of viscous symmetric instability, though their analysis did not distinguish between model grid types. The EEN vector-invariant discretization on the C grid displays too-large growth rates at small scales. Spurious instability using this discretization has been observed and discussed in a similar configuration (barotropic rather than sheared background velocity) by Hollingsworth et al. (1983) and Bell et al. (2017). Overall these behaviors confirm intuition: the C grid is more suited to the unbalanced symmetric instability than the B grid. The B grid with a grid size of 3.125 km achieves results similar to the C grid with a grid size of 6.25 km; in this case the B grid requires double the resolution to get results similar to the C grid. The qualitative behavior for a smaller deformation radius, and proportionally smaller grid sizes, is identical to that shown here.

4.2. B Grid Baroclinic Instability

Figure 2 shows growth rates of baroclinic instability at $Ri = 100$ for the B grid at grid sizes of $25, 12.5,$ and 6.25 km. At ‘eddy-permitting’ resolution of 25 km, the growth rate is on the order of 10% too small, but the growth rates and the range of unstable modes are both quite accurate at ‘eddy-resolving’ grid scales of 12.5 and 6.25 km. This same qualitative behavior occurs at all Richardson numbers from $1/2$ to $10,000$. The behavior off the baroclinic axis (i.e. $k_y \neq 0$, not shown) is qualitatively similar to the behavior shown here for $k_y = 0$. Since baroclinic instability is a source of eddy energy, we conjecture that the reduced growth rate of baroclinic instability at eddy-permitting resolution could lead to unrealistically-weak eddies at these resolutions.

4.3. C Grid Baroclinic Instability

Figure 3a shows growth rates of baroclinic instability at $Ri = 100$ for the C grid at grid sizes of $25, 12.5,$ and 6.25 km, and for perturbations on the baroclinic axis $k_y = 0$; the Nyquist wavenumber for each grid size has been marked with an \times . The behavior of the real instability is overshadowed by the appearance of a spurious instability at higher

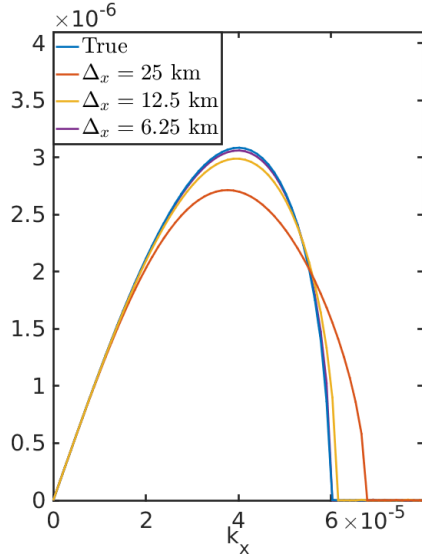


Figure 2: Growth rates of baroclinic instability at $Ri = 100$ on the B grid for grid sizes $\Delta_x = 25, 12.5,$ and 6.25 km. Growth rates are shown in units of s^{-1} ; the wavenumber k_x has units of m^{-1} . The blue line shows the true growth rate, obtained by taking $\Delta_x \rightarrow 0$. All results were computed using $N_z = 128$. The abscissa focuses on the behavior near the main instability; there is no instability at larger wavenumbers.

wavenumbers. The peak of the spurious instability always occurs near the Nyquist wavenumber, and the peak growth rate is unaffected by variation in Δ_x . At any fixed wavenumber k_x the spurious instability decays to 0 as $\Delta_x \rightarrow 0$, but for any Δ_x there is a wavenumber k_x that is spuriously unstable. The impact of vertical resolution was tested by re-computing the growth rates at $\Delta_x = 25$ km using $N_z = 512$; the growth rates are visually indistinguishable from those computed using $N_z = 128$.

The eigenvector associated with the peak of the spurious instability at $\Delta_x = 12.5$ km (shown as a black square in Fig. 3a) was computed and is shown in Fig. 3b–3d. Panels b, c, and d show the vertical profiles of the real (blue) and imaginary (red) parts of \hat{u} , \hat{v} , and \hat{b} , respectively. The profiles decay rapidly to zero for $z < 2000$ m. The amplitude of the profiles is immaterial, since they essentially correspond to an unstable direction in phase space; they have been normalized so that the maximum of $|\hat{v}|$ is 1. The spuriously-unstable modes come in pairs with the same growth rate, one for each boundary (not shown). The unstable modes are dominated by meridional (cross-front) velocity, with a weaker zonal (along-front) velocity. The buoyancy is approximately a factor of N smaller than the velocity, which is the same as for the primary Eady instability.

Figure 4 shows the scaled growth rate along the baroclinic axis for the C grid with $\Delta_x = 6.25$ km for a range of Richardson numbers from $1/2$ to 10^4 . The raw growth rate varies by over two orders of magnitude across this range of Richardson numbers, and Fig. 4 shows the growth rate multiplied by N/M^2 . In the limit of large Ri , the Eady baroclinic instability approaches a peak growth rate of approximately $0.31M^2/N$; this

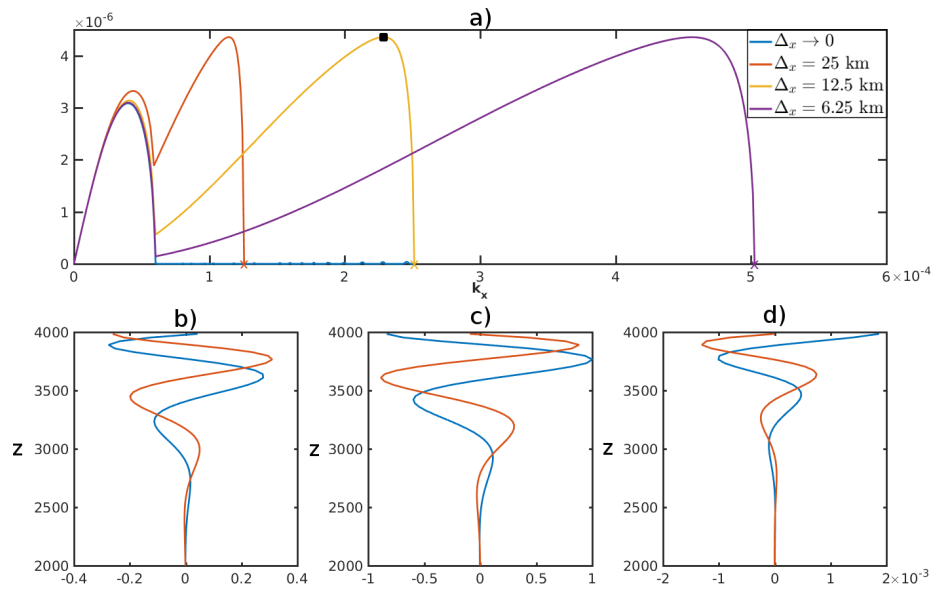


Figure 3: a) Growth rates of baroclinic instability at $Ri = 100$ on the C grid for grid sizes $\Delta_x = 25$, 12.5, and 6.25 km. Growth rates are shown in units of s^{-1} ; the wavenumber k_x has units of m^{-1} . The blue line shows the true growth rate, obtained by taking $\Delta_x \rightarrow 0$. All results were computed using $N_z = 128$. The abscissa extends to larger wavenumbers than in Fig. 2 to include the spurious instabilities present on the C grid. The Nyquist wavenumbers for grid sizes $\Delta_x = 25$, 12.5, and 6.25 km are marked with \times at the end of the growth rate curves. The eigenvector of the unstable mode shown with a black square in panel a) was computed; b) \hat{u} , c) \hat{v} , and d) \hat{b} . Blue and red lines in panels b)–d) are the real and imaginary components of the eigenvectors, respectively.

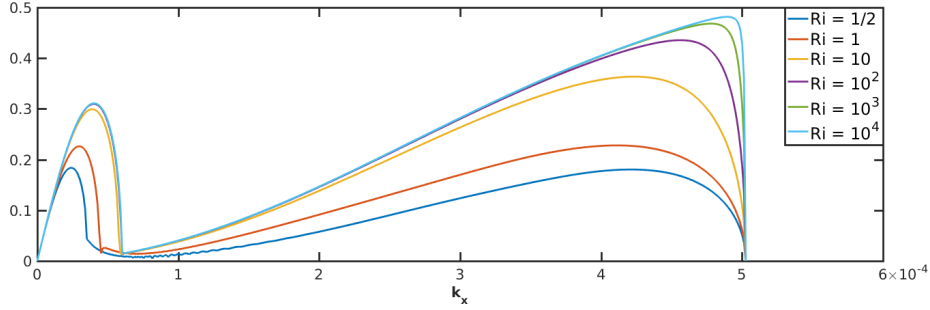


Figure 4: Scaled growth rates of baroclinic instability on the C grid $\Delta_x = 6.25$ km and Richardson numbers $1/2$ through 10^4 . Growth rates have been multiplied by N/M^2 which results in a non-dimensional growth rate; the wavenumber k_x has units of m^{-1} .

behavior is clearly seen for $k_x < 10^{-4}$. The amplitude of the spurious instability at large k_x scales similarly to the non-spurious Eady instability. In the limit of large Richardson numbers the peak of the spurious instability scales approximately as $M^2/(2N)$. At smaller Richardson numbers the growth rate is somewhat less than this, but across four orders of magnitude in Richardson number the maximum spurious growth rate is in the range $[0.2M^2/N, 0.5M^2/N]$. The growth rate of the spurious instability decays as k_y moves off of the baroclinic axis, just like the primary baroclinic instability (not shown).

4.4. Causes & Remedies

In this section tests are performed to attempt to isolate the cause of the spurious baroclinic instability on the C grid, and to suggest remedies. The most likely cause is the averaging that appears in the Coriolis terms on the C grid. This averaging is actually acting as a linear interpolation from the location of u to the location of v , and vice versa. It is possible to replace this second-order averaging approach with a perfect interpolation for normal modes; clearly this is not possible in general, but it serves to test whether Coriolis averaging is an essential cause of the spurious instability. The term $a_x^- a_y^+ \mathbf{u}'$ in Eq. (39) interpolates \mathbf{u}' west and north to the location of \mathbf{v}' . Similarly, the term $a_x^+ a_y^- \mathbf{v}'$ in Eq. (38) interpolates \mathbf{v}' east and south to the location of \mathbf{u}' . A normal mode has the following exact horizontal structure $e^{i(k_x \Delta_x i + k_y \Delta_y j)}$. To evaluate half a grid point west, one simply multiplies by $e^{-ik_x \Delta_x / 2}$, and similarly to move half a grid point north, south, or east. To test the impact of Coriolis averaging on the spurious instability we re-compute eigenvalues with this perfect Coriolis interpolation. Figure 5a shows the results of this calculation at $Ri = 100$ and $\Delta_x = 6.25$ km; while it does reduce the spurious instability at intermediate wavelengths, the growth rate near the Nyquist wavenumber is slightly worse. This suggests that interpolation schemes for the Coriolis force that are more accurate than the standard approach will not cure the spurious instability.

Although higher-order tracer advection schemes are more widely available in ocean models than higher-order momentum advection schemes, we test whether a fourth-order centered advection scheme applied to both tracers and momentum might cure

the spurious instability. This is implemented as follows: the second-order centered difference $a_x^+ \delta_x^-$ that appears in the terms $\bar{\mathbf{u}}(a_x^+ \delta_x^- \mathbf{u}')$ in Eq. (38), $\bar{\mathbf{u}}(a_x^+ \delta_x^- \mathbf{v}')$ in (39), and $\bar{\mathbf{u}}(a_x^+ \delta_x^- \mathbf{b}')$ in (40) is replaced with fourth-order centered difference approximation of the form

$$\delta_x^{(4)} \mathbf{u}' = \frac{\mathbf{u}'_{[i-2]} - 8\mathbf{u}'_{[i-1]} + 8\mathbf{u}'_{[i+1]} - \mathbf{u}'_{[i+2]}}{12\Delta_x}. \quad (47)$$

Figure 5a (yellow line) shows the results of this calculation at $\text{Ri} = 100$ and $\Delta_x = 6.25$ km. While fourth-order advection does reduce the spurious instability at intermediate wavelengths, the growth rate near the Nyquist wavenumber is essentially unchanged.

Although fourth-order momentum and tracer advection fail to significantly improve the spurious instability, we checked the impact of using fourth-order tracer advection but only second-order momentum advection. The results of this calculation are shown in Figure 5a (purple line). Surprisingly, the use of fourth-order advection on only the tracer field completely removes the spurious instability at intermediate wavelengths. The peak of the spurious instability near the Nyquist wavenumber is essentially unchanged.

Several other tests not reported here have failed to identify any single term in the equations that is primarily responsible for the existence of the spurious instability. It seems to result from a vicious collusion of the numerical errors present in several different terms in the equations. The behavior reported above holds qualitatively over a wide range of Richardson numbers.

Having failed to completely remove the spurious instability by improving the numerical approximations (though this may yet prove possible), attention is turned to methods for mitigating its effects. The obvious candidates to damp a spurious small-scale instability are viscosity and diffusion. First consider *vertical* viscosity and diffusion. The coefficient of vertical tracer diffusion is constrained to be small in ocean models to avoid spurious diapycnal mixing, so we will consider only vertical viscosity. The vertical scale of the spuriously-growing perturbations is not particularly small, as exemplified in Fig. 3b–d, and one should not expect vertical viscosity to be an effective means to damp the instability. It has been verified that the relatively large vertical viscosity of $\nu_z = 10^{-3}$ m²/s has minimal impact on the instability at $\text{Ri} = 100$ and $\Delta_x = 6.25$ km.

Since the peak growth rate of the spurious instability scales approximately as $M^2/(2N)$, one can simply choose viscous and diffusive coefficients large enough that the rate of viscous damping matches or exceeds the rate of spurious growth. The problem becomes easier to analyze if the coefficient of horizontal viscosity is set equal to that of horizontal diffusion, in which case the normal mode equations take the form

$$\frac{d}{dt} \begin{pmatrix} \hat{\mathbf{u}} \\ \hat{\mathbf{v}} \\ \hat{\mathbf{b}} \end{pmatrix} = (\mathbf{L} - \nu_h \hat{\mathbf{D}}) \begin{pmatrix} \hat{\mathbf{u}} \\ \hat{\mathbf{v}} \\ \hat{\mathbf{b}} \end{pmatrix} \quad (48)$$

where $\hat{\mathbf{d}}$ is the Fourier symbol of the horizontal diffusion operator. For example, apply-

ing the standard second-order Laplacian diffusion operator leads to

$$\hat{d} = \frac{4}{\Delta_x^2} \sin^2\left(\frac{k_x \Delta_x}{2}\right) + \frac{4}{\Delta_y^2} \sin^2\left(\frac{k_y \Delta_y}{2}\right). \quad (49)$$

To remove the spurious instability one can choose the viscous coefficient ν_h so that the peak growth rate of the spurious instability ($M^2/(2N)$) matches the damping rate of second-order discrete harmonic (Laplacian) or biharmonic diffusion at the Nyquist wavenumber. Let a harmonic viscosity by ν_2 and a biharmonic viscosity be ν_4 ; then the conditions are

$$\nu_2 \geq \frac{M^2 \Delta_x^2}{8N}, \quad \nu_4 \geq \frac{M^2 \Delta_x^4}{32N}. \quad (50)$$

Figure 5b compares the effect of harmonic and biharmonic damping and of fourth-order tracer advection on the growth rates. The parameters are $N = 10^{-3} \text{ s}^{-1}$, $M = 10^{-4} \text{ s}^{-1}$ and $\Delta_x = 6.25 \text{ km}$, and the viscosities have been chosen according to the criteria above, leading to $\nu_2 = 49 \text{ m}^2/\text{s}$ and $\nu_4 = 4.8 \times 10^8 \text{ m}^4/\text{s}$. Harmonic viscosity and diffusion are able to completely damp the spurious instability at all scales. At the reasonably-high resolution of $\Delta_x = 6.25 \text{ km}$ the true baroclinic growth rate is only slightly diminished, but at coarser scales the amount of dissipation necessary to stop the instability might be sufficient to detrimentally affect the primary instability.

Biharmonic viscosity is usually preferred over harmonic viscosity in eddying simulations because it helps confine unphysical dissipation to the smallest horizontal scales. Figure 5b shows that when using the standard second-order discretization of advection, biharmonic viscosity damps the spurious instability at the smallest scales but not at intermediate scales. This residual, weakly-growing spurious instability at intermediate scales is unsavory, and can be eliminated by using fourth-order tracer advection. The salutary combined effects of biharmonic viscosity and fourth-order tracer advection are shown in Fig. 5b.

It is clear from Fig. 5b that the viscosities prescribed in Eq. (50) are slightly larger than necessary to damp the spurious instability. The results in Fig. 4 indicate that this will be more pronounced at smaller Richardson numbers. Naturally, other considerations also conspire to set the value of viscous and diffusive coefficients in eddying ocean model simulations, and the prescriptions of Eq. (50) should be regarded as guidelines.

4.5. Comparison to nonlinear simulations

To verify that the linear stability analysis corresponds with the behavior of ocean models, we computed unstable perturbations from the linear instability analysis and introduced them as initial conditions in nonlinear simulations. The simulations were run using the MITgcm code (Marshall et al., 1997) in a horizontally-periodic domain of size $1200 \times 400 \times 4 \text{ km}$, with grid spacing 4 km in the horizontal and 100 uniformly-spaced vertical levels. The parameters of the background flow were set to $N^2 = 10^{-6} \text{ s}^{-2}$, $M^2 = 10^{-9} \text{ s}^{-2}$, and $f_0 = -10^{-4} \text{ s}^{-1}$. An initial perturbation was introduced with zonal wavelength of $4\Delta_x = 16 \text{ km}$ (i.e. with wavenumber equal to half the Nyquist wavenumber) and with vertical profile that yields the fastest linear growth for perturbations of that scale. The perturbation was normalized so that the maximum velocity was 0.1 cm/s . This perturbation has a wavelength that should be stable in the exact Eady

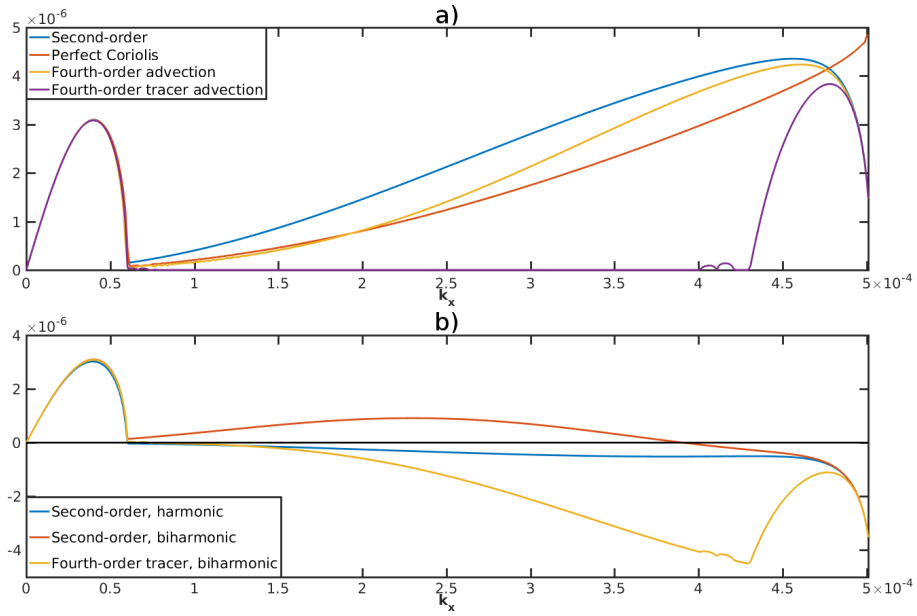


Figure 5: Growth rates of baroclinic instability at $Ri = 100$ on the C grid for $\Delta_x = 6.25$ km. Growth rates are shown in units of s^{-1} ; the wavenumber k_x has units of m^{-1} . a) Shows the growth rate obtained with the standard second-order configuration (blue), with perfectly-interpolated Coriolis terms (red), with fourth-order advection of tracers and momentum (yellow), and with fourth-order advection of tracers only (purple). b) Shows growth rates obtained with the standard configuration and harmonic (i.e. Laplacian) horizontal diffusion of momentum and tracers with $\nu_2 = 49$ m^2/s (blue), with the standard configuration and biharmonic horizontal diffusion of momentum and tracers with $\nu_4 = 4.8 \times 10^8$ m^4/s (red), and with the fourth-order tracer advection and biharmonic horizontal diffusion of tracers and momentum (same ν_4 ; yellow).

problem; by contrast, the linear stability analysis of the second-order C grid discretization predicts a growth rate of $2.18 \times 10^{-7} \text{ s}^{-1}$. The kinetic energy of the perturbations should thus grow at a rate of approximately $2 \times 2.18 \times 10^{-7} = 4.36 \times 10^{-7} \text{ s}^{-1}$. The nonlinear simulation was run for 100 days and the total kinetic energy was tracked; over this time period the total kinetic energy grew by a factor of more than 1000. The instantaneous growth rate of kinetic energy was estimated at each day using the formula

$$\text{KE Growth Rate} \approx \frac{1}{\tau} \ln \left(\frac{\text{KE}(t + \tau)}{\text{KE}(t)} \right)$$

where τ is one day and KE is the total kinetic energy. Figure 6a shows a time series of the estimated growth rate of kinetic energy; the computed growth rate is close to the value predicted by the linear theory, $4.36 \times 10^{-7} \text{ s}^{-1}$. After 250 days the growth is sufficient for nonlinear effects to appear, which ends the exponential growth. This simulation verifies the existence of a spurious linear instability in the C grid Eady problem.

The linear theory says that when fourth-order tracer advection is used, there are no eigenvalues with positive real part for perturbations with this wavelength. One could follow the procedure above by computing any eigenvector of the linear problem and introducing it as an initial perturbation to the nonlinear simulation, but this might be unsatisfying because the linear theory suggests that *any* perturbation with this wavelength is stable. In fact this suggestion – that having no unstable eigenvalues implies that no solutions will grow – is false, unless the linear system is *normal*. A complex matrix \mathbf{A} is ‘normal’ when it commutes with its complex-conjugate transpose, i.e. $\mathbf{A}\mathbf{A}^* = \mathbf{A}^*\mathbf{A}$. A normal matrix has a complete set of orthogonal eigenvectors, and the growth or decay of solutions to the linear system of differential equations $\dot{\mathbf{y}} = \mathbf{A}\mathbf{y}$ is determined completely by the eigenvalues of \mathbf{A} . The matrix \mathbf{L} in Eq. (46) is not normal (for the second-order, fourth-order, or exact systems), and therefore does not have a complete set of orthogonal eigenvectors. One of the ramifications of this fact is that solutions of the linear system can grow even when all the eigenvalues have non-positive real part. Non-normal behavior is common in fluid dynamics, and its presence in the quasigeostrophic Eady problem was noted by Farrell and Ioannou (1996).

The goal of this section is to verify the linear theory in a nonlinear simulation, not to perform a full generalized stability analysis in the vein of Farrell and Ioannou (1996). With that in mind, we introduced the same initial perturbation from the second-order simulation (described above) into a simulation using fourth-order tracer advection. The perturbation grows, but this is not a contradiction of the linear theory. The linear theory predicts that the instantaneous growth rate associated with this particular perturbation (the instantaneous growth rate is $\mathbf{y}^*(\mathbf{L} + \mathbf{L}^*)\mathbf{y}/\|\mathbf{y}\|^2$ where \mathbf{y} is the initial perturbation) is $4.36 \times 10^{-7} \text{ s}^{-1}$. The growth rate measured from the nonlinear simulation is shown in Fig. 6b. The first 100 days show wildly varying estimates of the linear growth rate, which then settles down to a value close to the theoretically-predicted value. This validates the linear theory while simultaneously illustrating the dangers of over-interpreting eigenvalues in non-normal systems.

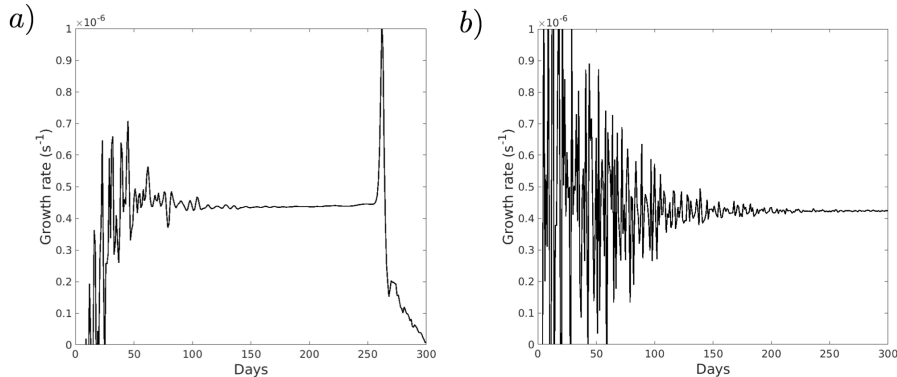


Figure 6: Growth rates of kinetic energy in nonlinear simulations initialized with the same small-amplitude perturbation. a) Second-order advection; the theoretically-predicted growth rate is $4.36 \times 10^{-7} \text{ s}^{-1}$. b) Fourth-order tracer advection; the theoretically-predicted growth rate is $4.36 \times 10^{-7} \text{ s}^{-1}$.

5. Conclusions

This paper investigates the effect of horizontal discretization on baroclinic and symmetric instabilities in the hydrostatic Eady problem. The effects of vertical discretization are minimized by using uniform, high resolution in the vertical; the effects of vertical discretization on baroclinic instability have been studied by Arakawa and Moorthi (1988), Bell and White (1988) and Bell and White (2017). In the horizontal, the standard flux-form energy-conserving second-order B and C grid discretizations are considered, along with the two forms of vector-invariant discretizations on the C grid. The flux-form and vector-invariant enstrophy-conserving ENS schemes (Maded, 2008) on the C grid give a better representation of symmetric instability than the B grid; the latter has growth rates that are generally too small. The vector-invariant enstrophy and energy conserving EEN scheme on the C grid (Arakawa and Lamb, 1981; Madec, 2008) has too-large growth rates for symmetric instability at small scales. This behavior is presumably related to the Hollingsworth instability (Hollingsworth et al., 1983) and the ‘symmetric instability of the computational kind’ discussed by Bell et al. (2017) and Ducouso et al. (2017).

The representation of baroclinic instability on the B grid is qualitatively correct at eddy-permitting and eddy-resolving resolutions. No spurious instabilities are observed, and the primary deficiency is that the growth rates can be on the order of 10% too small at eddy-permitting resolution. Since mesoscale eddies are energized by baroclinic instability, this suggests that eddies in a B grid model at eddy-permitting resolution might extract too little potential energy from the large scale flow, resulting in eddies that are too weak. This explanation for the weakness of eddies at eddy-permitting resolution is in stark contrast to the energetic picture assumed in many recent eddy-permitting parameterization studies that either assume that the missing energy comes from energetic backscatter from subgrid scales (Grooms and Majda, 2013; Kitsios et al., 2013; Grooms and Majda, 2014; Grooms et al., 2015b), or that the eddies are overly-damped by viscosity (Jansen and Held, 2014). The relative importance of anemic baroclinic

production, missing backscatter, and spurious dissipation in the energy budget of eddies at eddy-permitting resolution remains unknown.

A spurious baroclinic instability was discovered on the C grid, where the flux-form discretization and the two vector-invariant forms all give the same results. This spurious instability is peaked at scales just below the smallest resolvable (Nyquist) scale, but has relatively large vertical scales. The unstable perturbations manifest primarily in the velocity field (primarily cross-front), with a weak signature in the density field. The growth rates scale similarly to the baroclinic growth rate, with a peak growth rate of approximately $f_0/(2\sqrt{Ri})$ where Ri is the Richardson number. This growth rate is approximately independent of the grid scale Δ_x , and the spurious instability does not disappear as the grid is refined; instead, it simply moves to smaller scales. It was found that fourth-order centered tracer advection significantly improves the spurious instability, confining it to the very smallest scales but not significantly reducing its growth rate; curiously, using fourth-order momentum advection had little positive impact. Overall it is suggested that eddy-permitting and eddy-resolving models on the C grid should use fourth-order tracer advection with biharmonic viscosity and diffusion with coefficients $\nu_4, \kappa_4 \geq f_0\Delta_x^4/(32\sqrt{Ri})$. For mesoscale Richardson numbers on the order of 100 and eddy-resolving grid scales less than 10 km, this amount of dissipation is not excessive.

The lack of spurious baroclinic instability on the B grid suggests that B grid models might be more appropriate for eddy-permitting and eddy-resolving simulations, though perhaps not for simulations resolving submesoscales and smaller. Even on the B grid, higher-order numerics might improve eddy-permitting ocean models (though fourth-order tracer advection was not found to improve the growth rates). These models are defined by the fact that the eddy scales are not much larger than the grid scale. Low- and high-order methods all give similarly accurate results for scales that are well-resolved by the grid. Higher-order methods are distinguished by giving better approximations at intermediate scales that are partially-resolved by the grid (e.g. wavelengths four to six times the grid spacing), and seem naturally suited to eddy-permitting modeling. (Neither low- nor high-order methods give accurate approximations for very-small scales with wavelengths near twice the grid spacing.) Grooms et al. (2015a) recently found that an idealized eddy-permitting model with fourth-order numerics gave better short-time forecasting and data-assimilation performance than a model with second-order numerics, and that the improvement was comparable in magnitude to the improvement obtained by using improved subgrid-scale parameterizations.

The Eady baroclinic instability is a type of baroclinic instability not often seen in the ocean. Tulloch et al. (2011) find that baroclinic instability in oceans typically results from a change of sign of the mean potential vorticity gradient in the interior (Phillips-type), or of the combination of a surface shear and an interior mean potential vorticity gradient ('ocean-Charney'-type). The Eady problem is analyzed here because the coefficients in the linear perturbation equations are independent of the x and y coordinates. More realistic non-uniform vertical mean shear would, through geostrophic balance, result in linear perturbation equations with coefficients that depend on the y coordinate (this does not happen in the quasigeostrophic approximation), which prevents the use of a full normal mode expansion. Because of this mismatch between the character of the Eady problem and of baroclinic instability in the oceans, the behavior reported here should be extrapolated to more complex ocean models with caution.

Finally, the analysis here has focused on the two quadrilateral grid schemes most common in global ocean models, the Arakawa B and C grids. It is of interest to pursue a similar analysis on the hexagonal grid used in the MPAS ocean model (Ringler et al., 2013). The methods used by Thuburn (2008) to study free wave propagation on hexagonal grids may be adapted to the baroclinic instability problem, but the analysis is sufficiently complex that it merits a separate study.

Acknowledgements

I. Grooms is grateful to F. Bryan, and K. Lindsay for providing references on the discretizations used in the POP and MOM ocean models, and to A. Adcroft for suggesting useful directions of inquiry. The authors are also grateful to the two anonymous referees. W. Barham is supported by NSF grant DMS-1407340.

Appendix A. Normal Mode Equations

The way to eliminate hydrostatic pressure is the same on both the B and C grids. On both grids, the discrete hydrostatic balance for a normal mode may be expressed as a linear system in the form

$$-\frac{1}{\Delta_z} \begin{bmatrix} 1 & -1 & 0 & \cdots & 0 \\ 0 & 1 & -1 & 0 & \vdots \\ \vdots & & \ddots & \ddots & \vdots \\ 0 & \cdots & 0 & 1 & -1 \\ 1 & \cdots & & \cdots & 1 \end{bmatrix} \hat{\mathbf{p}} = \frac{1}{2} \begin{bmatrix} 1 & 1 & 0 & \cdots & 0 \\ 0 & 1 & 1 & 0 & \vdots \\ \vdots & & \ddots & & \vdots \\ 0 & \cdots & 0 & 1 & 1 \\ 0 & \cdots & 0 & \cdots & 0 \end{bmatrix} \hat{\mathbf{b}}. \quad (\text{A.1})$$

The first $N_z - 1$ of these equations encode Eq. (18), while the last ensures that the baroclinic pressure has no barotropic component. This allows us to eliminate the baroclinic pressure by an equation of the form

$$\hat{\mathbf{p}} = \mathbf{P} \hat{\mathbf{b}} \quad (\text{A.2})$$

where \mathbf{P} is a square matrix; the entries are available in closed form, but the expressions are unwieldy.

The vertical velocity is obtained by integrating the discrete incompressibility condition, which has different forms on the B and C grids. On the B grid we have

$$\frac{1}{\Delta_z} \begin{bmatrix} 1 & 0 & \cdots & \cdots & 0 \\ -1 & 1 & 0 & & \vdots \\ \vdots & & \ddots & \ddots & \vdots \\ 0 & \cdots & & 1 & 0 \\ 0 & \cdots & 0 & -1 & 1 \end{bmatrix} \hat{\mathbf{w}} = -\hat{a}_y^- \hat{\delta}_x^- \hat{\mathbf{u}} - \hat{a}_x^- \hat{\delta}_y^- \hat{\mathbf{v}} \quad (\text{A.3})$$

and on the C grid

$$\frac{1}{\Delta_z} \begin{bmatrix} 1 & 0 & \cdots & \cdots & 0 \\ -1 & 1 & 0 & & \vdots \\ \vdots & & \ddots & \ddots & \vdots \\ 0 & \cdots & & 1 & 0 \\ 0 & \cdots & 0 & -1 & 1 \end{bmatrix} \hat{\mathbf{w}} = -\hat{\delta}_x^- \hat{\mathbf{u}} - \hat{\delta}_y^- \hat{\mathbf{v}}. \quad (\text{A.4})$$

The inverse of this coefficient matrix is available in closed form; it is Δ_z times a lower-triangular matrix whose diagonal and sub-diagonal elements are all ones. The vertical velocity only appears in the linear perturbation equations in the form $a_z^+ \hat{\mathbf{w}}$, so we will write

$$a_z^+ \hat{\mathbf{w}} = -\mathbf{W}(\hat{a}_y^- \hat{\delta}_x^- \hat{\mathbf{u}} - \hat{a}_x^- \hat{\delta}_y^- \hat{\mathbf{v}}) \quad (\text{A.5})$$

on the B grid and

$$a_z^+ \hat{\mathbf{w}} = -\mathbf{W}(\hat{\delta}_x^- \hat{\mathbf{u}} - \hat{\delta}_y^- \hat{\mathbf{v}}) \quad (\text{A.6})$$

on the C grid where the matrix \mathbf{W} is, in both cases,

$$\frac{\Delta_z}{2} \begin{bmatrix} 1 & 0 & \cdots & \cdots & 0 \\ 2 & 1 & 0 & & \vdots \\ \vdots & \ddots & \ddots & \ddots & \vdots \\ 2 & \cdots & 2 & 1 & 0 \\ 2 & \cdots & \cdots & 2 & 1 \end{bmatrix}. \quad (\text{A.7})$$

It remains to eliminate the barotropic pressure $\hat{\phi}$. The barotropic pressure is depth-independent, so it appears in the equations as a scalar coefficient multiplying a vector of all ones: $\mathbf{1}$. The normal mode momentum equations on the B grid, without having

eliminated $\hat{\phi}$, are

$$\begin{aligned} \frac{d\hat{\mathbf{u}}}{dt} = & - \left(\hat{a}_x^+ \hat{\delta}_x^- \mathbf{U} + \frac{M^2 \hat{a}_x^+ \hat{a}_y^+ \hat{a}_y^- \hat{\delta}_x^-}{f_0} \mathbf{W} \right) \hat{\mathbf{u}} \\ & + \left(- \frac{M^2 \hat{a}_x^+ \hat{a}_x^- \hat{a}_y^+ \hat{\delta}_y^-}{f_0} \mathbf{W} + f_0 \mathbf{I} \right) \hat{\mathbf{v}} \\ & - \hat{a}_y^+ \hat{\delta}_x^+ (\mathbf{P}\hat{\mathbf{b}} + \mathbf{1}\hat{\phi}) \end{aligned} \quad (\text{A.8})$$

$$\begin{aligned} \frac{d\hat{\mathbf{v}}}{dt} = & - f_0 \mathbf{I} \hat{\mathbf{u}} - \hat{a}_x^+ \hat{\delta}_x^- \mathbf{U} \hat{\mathbf{v}} \\ & - \hat{a}_x^+ \hat{\delta}_y^+ (\mathbf{P}\hat{\mathbf{b}} + \mathbf{1}\hat{\phi}) \end{aligned} \quad (\text{A.9})$$

where \mathbf{U} is a diagonal matrix with entries $\bar{\mathbf{u}}$. Following the derivation for the continuous case, the equations are first averaged across depth by multiplying from the left by $\mathbf{1}^T/N_z$ where T indicates the transpose. This eliminates the baroclinic pressure. Next, $\hat{\phi}$ is obtained by enforcing the condition $\mathbf{1}^T \left(\frac{d}{dt} \right) (\hat{a}_y^- \hat{\delta}_x^- \hat{\mathbf{u}} + \hat{a}_x^- \hat{\delta}_y^- \hat{\mathbf{v}}) = 0$. This leads to

$$\begin{aligned} \hat{\phi} = & - \frac{\mathbf{1}^T}{N_z (\hat{a}_x^+ \hat{a}_x^- \hat{\delta}_x^+ \hat{\delta}_x^- + \hat{a}_y^+ \hat{a}_y^- \hat{\delta}_y^+ \hat{\delta}_y^-)} \left[\right. \\ & \left(\hat{a}_x^+ \hat{a}_y^- (\hat{\delta}_x^-)^2 \mathbf{U} + \frac{M^2 \hat{a}_x^+ \hat{a}_y^+ (\hat{a}_y^- \hat{\delta}_x^-)^2}{f_0} \mathbf{W} + f_0 \hat{a}_x^- \hat{\delta}_y^- \mathbf{I} \right) \hat{\mathbf{u}} + \\ & \left. \left(\hat{a}_x^+ \hat{a}_x^- \hat{\delta}_x^- \hat{\delta}_y^- \mathbf{U} + \frac{M^2 \hat{a}_x^+ \hat{a}_x^- \hat{a}_y^+ \hat{a}_y^- \hat{\delta}_x^- \hat{\delta}_y^-}{f_0} \mathbf{W} - f_0 \hat{a}_y^- \hat{\delta}_x^- \mathbf{I} \right) \hat{\mathbf{v}} \right]. \end{aligned} \quad (\text{A.10})$$

The C grid expression is similarly derived, and for the flux-form and ENS vector-invariant forms is

$$\begin{aligned} \hat{\phi} = & - \frac{\mathbf{1}^T}{N_z (\hat{\delta}_x^+ \hat{\delta}_x^- + \hat{\delta}_y^+ \hat{\delta}_y^-)} \left[\right. \\ & \left(\hat{a}_x^+ (\hat{\delta}_x^-)^2 (\mathbf{U} + \frac{M^2}{f_0} \mathbf{W}) + f_0 \hat{a}_x^- \hat{a}_y^+ \hat{\delta}_y^- \mathbf{I} \right) \hat{\mathbf{u}} + \\ & \left. \left(\hat{a}_x^+ \hat{\delta}_x^- \hat{\delta}_y^- (\mathbf{U} + \frac{M^2}{f_0} \mathbf{W}) - f_0 \hat{a}_x^+ \hat{a}_y^- \hat{\delta}_x^- \mathbf{I} \right) \hat{\mathbf{v}} \right]. \end{aligned} \quad (\text{A.11})$$

The expression for the C grid EEN vector-invariant form is similarly derived.

In lieu of a summary explicitly detailing the entries of the matrix \mathbf{L} , we have provided in the supplementary material two Matlab scripts to construct the matrices, one script for the B grid and one for the C grid.

Arakawa, A., Lamb, V.R., 1977. Computational design of the basic dynamical processes of the UCLA general circulation model. *Methods in computational physics* 17, 173–265.

- Arakawa, A., Lamb, V.R., 1981. A potential enstrophy and energy conserving scheme for the shallow water equations. *Monthly Weather Review* 109, 18–36.
- Arakawa, A., Moorthi, S., 1988. Baroclinic instability in vertically discrete systems. *J. Atmos. Sci.* 45, 1688–1708.
- Bachman, S.D., Taylor, J.R., 2014. Modelling of partially-resolved oceanic symmetric instability. *Ocean Model.* 82, 15–27.
- Bell, M., White, A., 1988. Spurious stability and instability in n-level quasi-geostrophic models. *J. Atmos. Sci.* 45, 1731–1738.
- Bell, M.J., Peixoto, P.S., Thuburn, J., 2017. Numerical instabilities of vector-invariant momentum equations on rectangular c-grids. *Quarterly Journal of the Royal Meteorological Society* 143, 563–581.
- Bell, M.J., White, A.A., 2017. Analytical approximations to spurious short-wave baroclinic instabilities in ocean models. *Ocean Model.* 118, 31–40.
- Bryan, K., 1969. A numerical method for the study of the circulation of the world ocean. *J. Comp. Phys.* 4, 347–376.
- Charney, J.G., Fjørtoft, R., Neumann, J.v., 1950. Numerical integration of the barotropic vorticity equation. *Tellus* 2, 237–254.
- Delworth, T.L., Rosati, A., Anderson, W., Adcroft, A.J., Balaji, V., Benson, R., Dixon, K., Griffies, S.M., Lee, H.C., Pacanowski, R.C., Vecchi, G.A., Wittenberg, A.T., Zeng, F., Zhang, R., 2012. Simulated climate and climate change in the GFDL CM2.5 high-resolution coupled climate model. *J. Climate* 25, 2755–2781.
- Ducouso, N., Le Sommer, J., Molines, J.M., Bell, M., 2017. Impact of the symmetric instability of the computational kind at mesoscale-and submesoscale-permitting resolutions. *Ocean Modelling* 120, 18–26.
- Dukowicz, J.K., 1995. Mesh effects for Rossby waves. *J. Comp. Phys.* 119, 188–194.
- Eady, E., 1949. Long waves and cyclone waves. *Tellus* 1, 33–52.
- Farrell, B.F., Ioannou, P.J., 1996. Generalized stability theory. Part I: Autonomous operators. *J. Atmos. Sci.* 53, 2025–2040.
- Ferrari, R., Wunsch, C., 2009. Ocean circulation kinetic energy: Reservoirs, sources, and sinks. *Annual Review of Fluid Mechanics* 41.
- Frenger, I., Gruber, N., Knutti, R., Münnich, M., 2013. Imprint of Southern Ocean eddies on winds, clouds, and rainfall. *Nat. Geosci.* 6, 608–612.
- Gent, P.R., Danabasoglu, G., Donner, L.J., Holland, M.M., Hunke, E.C., Jayne, S.R., Lawrence, D.M., Neale, R.B., Rasch, P.J., Vertenstein, M., Worley, P.H., Yang, Z.L., Zhang, M., 2011. The Community Climate System Model version 4. *J. Climate* 24, 4973–4991.

- Graham, T., 2014. The importance of eddy permitting model resolution for simulation of the heat budget of tropical instability waves. *Ocean Model.* 79, 21–32.
- Grooms, I., Lee, Y., Majda, A., 2015a. Ensemble filtering and low-resolution model error: covariance inflation, stochastic parameterization, and model numerics. *Monthly Weather Review* 143, 3912–3924.
- Grooms, I., Lee, Y., Majda, A.J., 2015b. Numerical schemes for stochastic backscatter in the inverse cascade of quasigeostrophic turbulence. *Multiscale Modeling & Simulation* 13, 1001–1021.
- Grooms, I., Majda, A.J., 2013. Efficient stochastic superparameterization for geophysical turbulence. *Proc. Natl. Acad. Sci. USA* 110. doi:10.1073/pnas.1302548110.
- Grooms, I., Majda, A.J., 2014. Stochastic superparameterization in quasigeostrophic turbulence. *J. Comp. Phys.* 271. doi:DOI:10.1016/j.jcp.2013.09.020.
- Haidvogel, D.B., Beckmann, A., 1999. Numerical ocean circulation modeling. volume 2. World Scientific.
- Hallberg, R., 2013. Using a resolution function to regulate parameterizations of oceanic mesoscale eddy effects. *Ocean Model.* 72, 92–103.
- Hollingsworth, A., Kållberg, P., Renner, V., Burridge, D., 1983. An internal symmetric computational instability. *Quarterly Journal of the Royal Meteorological Society* 109, 417–428.
- Hurrell, J.W., Holland, M.M., Gent, P.R., Ghan, S., Kay, J.E., Kushner, P.J., Lamarque, J.F., Large, W.G., Lawrence, D., Lindsay, K., Lipscomb, W.H., Long, M.C., Mahowald, N., Marsh, D.R., Neale, R.B., Rasch, P., Vavrus, S., Vertenstein, M., Bader, D., Collins, W.D., Hack, J.J., Kiehl, J., Marshall, S., 2013. The community earth system model: A framework for collaborative research. *Bulletin of the American Meteorological Society* 94, 1339–1360.
- Jansen, M.F., Held, I.M., 2014. Parameterizing subgrid-scale eddy effects using energetically consistent backscatter. *Ocean Model.* 80, 36–48.
- Kirtman, B., Bitz, C., Bryan, F., Collins, W., Dennis, J., Hearn, N., Kinter III, J., Loft, R., Rousset, C., Siqueira, L.e.a., 2012. Impact of ocean model resolution on CCSM climate simulations. *Clim. Dynam.* 39, 1303–1328.
- Kitsios, V., Frederiksen, J., Zidikheri, M., 2013. Scaling laws for parameterisations of subgrid eddy–eddy interactions in simulations of oceanic circulations. *Ocean Model.* 68, 88–105.
- Le Sommer, J., Penduff, T., Theetten, S., Madec, G., Barnier, B., 2009. How momentum advection schemes influence current-topography interactions at eddy permitting resolution. *Ocean Model.* 29, 1–14.
- Lorenz, E.N., 1960. Energy and numerical weather prediction. *Tellus* 12, 364–373.

- Madec, G., 2008. NEMO ocean engine. Note du Pôle de modélisation, Institut Pierre-Simon Laplace (IPSL), France, No 27, ISSN No 1288-1619.
- Maltrud, M.E., McClean, J.L., 2005. An eddy resolving global $1/10^\circ$ ocean simulation. *Ocean Model.* 8, 31–54.
- Marshall, J., Adcroft, A., Hill, C., Perelman, L., Heisey, C., 1997. A finite-volume, incompressible Navier-Stokes model for studies of the ocean on parallel computers. *Journal of Geophysical Research: Oceans* 102, 5753–5766.
- Ringler, T., Petersen, M., Higdon, R.L., Jacobsen, D., Jones, P.W., Maltrud, M., 2013. A multi-resolution approach to global ocean modeling. *Ocean Model.* 69, 211–232.
- Sadourny, R., 1975. The dynamics of finite-difference models of the shallow-water equations. *J. Atmos. Sci.* 32, 680–689.
- Shchepetkin, A.F., McWilliams, J.C., 2005. The regional oceanic modeling system (ROMS): a split-explicit, free-surface, topography-following-coordinate oceanic model. *Ocean Model.* 9, 347–404.
- Stone, P.H., 1966. On non-geostrophic baroclinic stability. *J. Atmos. Sci.* 23, 390–400.
- Stone, P.H., 1970. On non-geostrophic baroclinic stability: Part II. *J. Atmos. Sci.* 27, 721–726.
- Thuburn, J., 2008. Numerical wave propagation on the hexagonal C-grid. *J. Comp. Phys.* 227, 5836–5858.
- Treguier, A., Deshayes, J., Le Sommer, J., Lique, C., Madec, G., Penduff, T., Molines, J., Barnier, B., Bourdalle-Badie, R., Talandier, C., 2014. Meridional transport of salt in the global ocean from an eddy-resolving model. *Ocean Sci.* 10, 243–255.
- Tulloch, R., Marshall, J., Hill, C., Smith, K.S., 2011. Scales, growth rates, and spectral fluxes of baroclinic instability in the ocean. *J. Phys. Ocean.* 41, 1057–1076.
- Wajsowicz, R.C., 1986. Free planetary waves in finite-difference numerical models. *J. Phys. Ocean.* 16, 773–789.